RESEARCH ARTICLE | JANUARY 13 2025

Heat-powered IoT node: A synergistic fusion of thermoacoustic engine and triboelectric nanogenerator

Yizhou Li ; Yawei Wang ; Yihao Li ; Xuzhang Peng ; Dian Li; Xin Xia ; Xin Li; Yunlong Zi; Guobiao Hu

Appl. Phys. Lett. 126, 023902 (2025)
https://doi.org/10.1063/5.0244410

Applied Physics Letters ARTICLE pubs.aip.org/aip/apl

Heat-powered IoT node: A synergistic fusion of thermoacoustic engine and triboelectric nanogenerator

Cite as: Appl. Phys. Lett. **126**, 023902 (2025); doi: 10.1063/5.0244410
Submitted: 18 October 2024 · Accepted: 27 December 2024 ·
Published Online: 13 January 2025

View Online Export Citation CrossMark

Yizhou Li,[1] Yawei Wang,[1] Yihao Li,[1] Xuzhang Peng,[1] Dian Li,[1] Xin Xia,[2] Xin Li,[3] Yunlong Zi,[2] and Guobiao Hu[1,a)]

AFFILIATIONS

[1]Thrust of Internet of Things, The Hong Kong University of Science and Technology (Guangzhou), Nansha, Guangzhou 511400, Guangdong, China
[2]Thrust of Sustainable Energy and Environment, The Hong Kong University of Science and Technology (Guangzhou), Nansha, Guangzhou 511400, Guangdong, China
[3]Guangzhou Institute of Technology, Xidian University, Guangzhou, Guangdong, China

[a)]**Author to whom correspondence should be addressed:** guobiaohu@hkust-gz.edu.cn

ABSTRACT

This study presents the design and analysis of a thermal energy harvester that integrates a thermoacoustic engine (TAE) with a honeycomb-structured triboelectric nanogenerator (H-TENG), referred to as TAEH-TENG. This design is specifically developed to demonstrate the potential of thermal energy harvesting for low-power Internet of Things (IoT) applications. By leveraging the high energy conversion efficiency of TAEs and the exceptional robustness of H-TENGs, this harvester overcomes the limitations of traditional designs, which often involve complex or costly components. The experimental results revealed the oscillation characteristics of the TAEH-TENG: by utilizing a hot heat exchanger (HHE) with a length of 10 cm, the system can sustain oscillation over 150–350 °C. Furthermore, the harvester is capable of generating an open-circuit voltage of 25 V, an RMS current of 0.98 μA, and a peak power output of 0.48 mW, representing the highest power output achieved to date in comparison to previous studies. To further showcase the harvester's capability, an ultra-low-power IoT node was developed. Solely powered by the TAEH-TENG, the IoT node achieved cold-start, conducted *in situ* temperature measurement five times, and transmitted the data via Bluetooth within 120 s. This study not only showcases a fully self-powered IoT application but, more importantly, significantly advances the technology beyond the previous limitations faced by thermoacoustic and triboelectric integrations. By demonstrating the capability to power an ultra-low-power IoT node, this research highlights the TAEH-TENG's potential for practical, real-world energy solutions, marking a significant milestone in the deployment of heat-powered IoT applications.

The growing concerns about environmental sustainability and energy shortage crises have intensified the demand for exploring and exploiting renewable energy sources.[1,2] Among various renewable energy sources, thermal energy is always overlooked,[3] despite its substantial potential for sustainable development. This oversight can largely be attributed to the limited applicability and immaturity of current thermal energy harvesting technologies.[4,5] In recent years, thermoacoustic energy harvesters have emerged as a promising method for effectively exploiting thermal energy sources, providing alternative systems for harvesting thermal energy in niche applications.[6,7] A typical thermoacoustic energy harvester consists of a thermoacoustic engine (TAE) and an acoustic-to-electric transducer/converter.[8] Thermoacoustic engines are capable of converting thermal energy into acoustic energy,[9] and the transducers can transform acoustic energy into electricity.[10] Given that TAEs operate as external combustion engines, this technology can exploit a wide variety of heat sources, such as low-quality industrial waste heat,[11–13] outdoor solar radiation,[14] geothermal heat,[7] etc. Most TAEs used electromagnetic components such as linear alternators[15] or loudspeakers[16] to convert acoustic energy into electricity. Other techniques/components like magnetohydrodynamic devices[17] and bidirectional turbines[18] have also been utilized in practical applications. Despite their potential for large-scale power generation, these technologies face significant obstacles, particularly in the demand for high-performance materials,[19–21] reliability concerns, and challenges in related high-tech

manufacturing.[22,23] Moreover, their complex structures/systems and manufacturing processes pose difficulties in fabrication and scalability, thus restricting their wide applications.

In this context, piezoelectric materials [24,25] and triboelectric nanogenerators (TENGs)[26–28] have emerged as alternative approaches for developing small-scale energy harvesting systems. While effective at high frequencies and well-suited for compact TAEs,[24] most piezoelectric transducers are fragile and brittle, compromising the operational lifespan.[29] On the other hand, TENGs based on triboelectrification and electrostatic induction offer high robustness,[30,31] remarkable power density,[32,33] ease of fabrication,[34] and robust integration capabilities.[35] Hence, TENGs hold great potential in powering small-scale appliances. Zhu *et al.* first proposed a thermoacoustic-driven TENG that could generate a maximum voltage of 10 V and a power of 0.008 μW at a 400 MΩ load.[36] They further advanced their research by employing liquid metal as both the triboelectric and resonant material in a standing-wave TAE, and an improved open-circuit voltage of 15 V was achieved.[37] Ahmed *et al.* conducted detailed modeling and analysis of a TENG-attached-THE. Their simulations well aligned with experimental results.[38]

While the feasibility and potential of TAE-TENGs have been proven by prior studies, previous designs suffer from low power outputs, and none have convincingly demonstrated TAE-TENGs' practicality for real-world applications. The shortcomings can be attributed to three primary reasons. The first reason is that the integration with the TENG altered the TAE's original structure, deteriorating the efficiency due to changed boundary conditions.[39] The second reason is that some studies[36,38] utilized air as the resonant medium, leading to the system operating at high frequencies that are not well-suited for TENGs,[40] which perform more effectively with low-frequency, large-amplitude vibrations. The third reason is that using air as the resonant medium operates at ambient pressure, which significantly limits the compression ratio and, as a result, reduces overall efficiency.[41] According to the literature review and the identified research gap, there is a pressing need for a study that firmly demonstrates the TAE-TENG system's ability to not only achieve high efficiency and power output but also possess practical application potential. This study aims to fill the above research gap by presenting a thermoacoustic engine (TAE) integrated with a honeycomb-structured triboelectric nanogenerator (H-TENG), referred to as TAEH-TENG hereinafter. This design intends to overcome the above limitations from the following aspects:

(i) Introducing a solid piston to replace a long resonance tube to couple with the TAE: this enhances efficiency due to a higher compression ratio achieved by piston movement,[41] as compared to systems operating at ambient pressure.[36,38] Additionally, the use of a solid piston as the resonant medium in place of air eliminates the need for a long resonance tube and enhances power density.[42] Moreover, this change leads to lower thermoacoustic oscillation frequencies and higher power outputs,[37,41,43] making it more suitable for TENG integration.[40]
(ii) Implementing a honeycomb-structured TENG (H-TENG)[44] as the generator within the solid piston: this compact design greatly enhances energy harvesting efficiency. The honeycomb configuration maximizes surface area for effective charge transfer. Utilizing polytetrafluoroethylene (PTFE) balls as the dielectric layer improves the H-TENG's performance and actuation capabilities. Furthermore, its structural design allows for easy integration and stacking within the solid piston, maintaining the system's simplicity and adherence to original boundary conditions, thereby addressing the issues identified in previous research.

In this study, a comprehensive analysis and discussion of the electrical performance tests were conducted. The TAEH-TENG system demonstrates an open-circuit voltage of 25 V, RMS current of 0.98 μA, and instantaneous power of 0.48 mW. An experiment was performed with a TAE incorporating four H-TENGs to charge capacitors, showcasing the output performance of the H-TENG. Furthermore, we built a comprehensive test platform designed to evaluate the real-world capabilities of the TAEH-TENG. Among its features, the platform includes an ultra-low-power IoT node equipped with a temperature sensor (TS) and Bluetooth Low Energy (BLE) module, specifically designed to showcase the potential for practical application. In addition, a receiving end is prepared to capture and upload signals from the IoT node to the cloud, ensuring efficient data communication. The TAEH-TENG cold-started the IoT node during the test, validating its deployment capability for heat-powered IoT applications. Based on the findings from the literature review, no previous studies have investigated a TAE-TENG system with coupling achieved through a solid piston. Furthermore, none of the prior TAE-TENG systems have demonstrated practical capabilities for powering real devices other than LED bulbs. Therefore, the proposed configuration marks a TAE-TENG system that is highly efficient, compact, and practical.

The experimental setup depicted in Fig. 1(a) is prepared for testing the TAEH-TENG comprising a TAE and a H-TENG. The TAE consists of a hot heat exchanger (HHE), a stack, and an ambient heat exchanger (AHE). The HHE is made of a quartz tube with the right end closed and the left end connected to the stack. The internal velvet acts as a heat buffer to store external heat, as shown in the inset. The aluminum stack, located between the HHE and AHE, is utilized to generate a temperature gradient to induce the oscillation of the compressible fluid. The AHE, made of a quartz tube and sealed at the left end by the solid piston, is exposed to the external environment at a temperature of 25 °C to radiate waste heat from the heater. An infrared (IR) camera (Fluke TiS55+) is used to monitor and visualize the temperature field changes around the heater. Its operation range is from −20 to 550 °C with an accuracy of ±2 °C (or ±2% of the digital readout). The output signals, including the open-circuit voltage, short-circuit current, and transfer charges, are measured using a Keithley 6514 electrometer, and the data are displayed and recorded in a custom LabVIEW VI application on a laptop. Figure 1(b) shows the components of the solid piston, including a piston sleeve, a piston cap, and a H-TENG unit. Specifically, the H-TENG consists of a circular honeycomb frame, PTFE balls, and copper electrodes. The fused deposition modeling (FDM) 3D printing technology is used to manufacture the honeycomb frame and the substrate of the copper electrodes. Following the additive manufacturing process, PTFE balls are inserted into the honeycomb structure, and a copper foil is affixed to one side of the electrode substrate. The honeycomb frame is positioned between the two copper electrodes to form a sandwich structure. The inset shows the installed solid piston and the key parameters of the TAE and H-TENG are listed in Table I.

Figure 1(c) depicts the working process of the TAE with an H-TENG unit, highlighting the interplay between thermal expansion, contraction, and piston movement across three stages. At the outset, the heater warms the HHE section, generating a temperature gradient

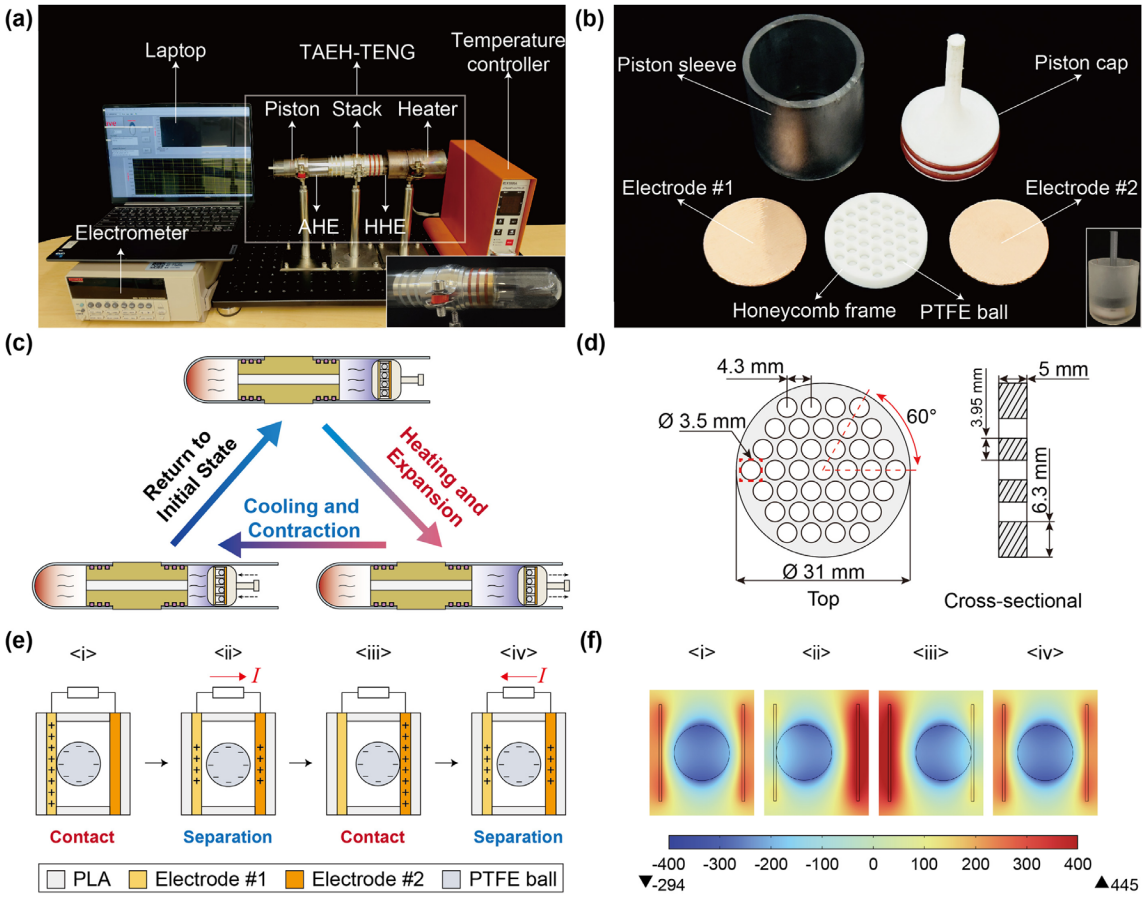

FIG. 1. (a) Experimental setup for testing the TAE and H-TENG. (b) The components of the solid piston with one H-TENG unit. (c) The operating cycle of the TAE with one H-TENG unit. (d) Schematic diagram of the honeycomb structure. (e) Working mechanisms of the H-TENG. (f) The electric potential distribution within the microstructure of the H-TENG with the PTFE ball positioned at different locations, as simulated using COMSOL Multiphysics.

that extends through the stack to the AHE. Subsequently, the thermal expansion of the compressible fluid occurs, propelling the piston to move rightward. Once the absorbed energy of the fluid reaches its maximum, the piston reaches its maximum displacement. As the gas cools down due to the heat transfer in the AHE, a pressure drop occurs, prompting gas contraction to pull the piston back to its initial position. In the final stage, the gas fully cools, contracts, and brings the piston to its original position, thus concluding the cycle and readying the system for a next round of expansion and contraction. In this process, the movement of the piston is directly influenced by the thermal condition of the gas in the tube. Figure 1(d) displays the schematic diagram of the honeycomb structure of the H-TENG from both the top and cross-sectional views. The diameter of the honeycomb is 31 mm, and each hole within the honeycomb has a diameter of 3.5 mm to facilitate smooth movement of the PTFE balls. The 60° orientation in this structure leads to a hexagonal close-packing arrangement, which is the most efficient way to pack circles in a plane. This configuration optimizes the effective contact area, which is essential for enhancing the energy harvesting efficiency of the H-TENG.

Figure 1(e) illustrates the working mechanism of the H-TENG unit, involving triboelectrification and electrostatic induction. In the triboelectrification process, electron transfer occurs at the contact interface due to the contact-separate motion, resulting in negative charges induced on the PTFE ball. In the electrostatic induction, an equal amount of reverse charge is induced on electrode #1 when the PTFE ball contacts it [Fig. 1(e-i)]. As the ball moves in the right direction [Fig. 1(e-ii)], the redistribution of induced electrons generates a current flowing to the right in the external circuit until the PTFE ball contacts with electrode #2 [Fig. 1(e-iii)]. Similarly, a leftward current is produced when the ball moves back to the left [Fig. 1(e-iv)]. Therefore, the oscillation of the PTFE ball produces an alternating current, converting kinetic energy into electricity. More details of this repetitive cycle of motion and charge transfer can be explained by the theoretical principles of the freestanding contact-mode TENG.[45] The governing equation for the H-TENG can be expressed as

$$V = -\frac{Q}{C} + V_{OC} = -\frac{(d_0 + g)}{\varepsilon_0 S} Q + \frac{2\sigma x}{\varepsilon_0}, \tag{1}$$

where V_{OC} and Q represent the open-circuit voltage and transfer charge, respectively, while C denotes the capacitance. The term d_0 corresponds to the effective dielectric thickness, and g stands for the total air gap between the two parallel electrode layers, which is also

TABLE I. The geometric parameters of the TAEH-TENG.

Components	Parameters	Values
Thermoacoustic engine	Length of HHE	10 cm
	Inner diameter of HHE	4 cm
	Length of aluminum stack	9.8 cm
	Outer diameter of aluminum stack	4.5 cm
	Diameter of through-hole in aluminum stack	1 cm
	Length of AHE	13 cm
	Inner diameter of AHE	3.605 cm
Piston and H-TENG	Length of piston sleeve	4 cm
	Inner diameter of piston sleeve	3.2 cm
	Length of power piston	5 cm
	Diameter of power piston	3.05 cm
	Thickness of electrode	0.1 cm
	Diameter of electrode	3 cm
	Thickness of honeycomb frame	0.5 cm
	Diameter of honeycomb frame	3 cm
	Number of holes in honeycomb	37

equivalent to the thickness of the honeycomb frame in the H-TENG. Furthermore, ε_0 represents the dielectric constant in a vacuum, S is the area of the copper electrode layer, x is the separation distance between the electrode layer and the surface of the PTFE ball, and σ refers to the charge density. The potential distribution within the H-TENG was simulated using COMSOL Multiphysics, and the results are presented in Fig. 1(f). It quantitatively demonstrates how the electric potential distribution varies in response to the varying position of the PTFE ball. Each panel in Fig. 1(f) shows the PTFE ball in a distinct position relative to the electrodes, corresponding to the states depicted in Fig. 1(e). The simulation result also reveals how change in the ball's position affects the voltage, aligned with Eq. (1), underscoring the dynamic changes in potential distribution throughout the operational cycle.

Given that the length of the HHE and the heating temperature are critical factors affecting the performance of a TAE,[41,43,46] the relationship between the HHE length and the oscillation onset temperature of the TAE is investigated. The results are shown in Fig. 2. Thermal images from axial and radial perspectives displayed on the right side of Fig. 2 illustrate temperature distributions within the TAE at different heating temperatures. The symbols on the left indicate the operational status: green check marks (√) denote successful oscillation, while red crosses (×) signify failures. The experimental results reveal that the HHE with a length of 10 cm can sustain the oscillation over a wide temperature range (from 150 to 350 °C). The oscillation onset temperature rises to 250 and 350 °C when the HHE's length extends to 20 and 30 cm, respectively. The thermal images of the HHE from the axial and radial directions of the entire setup are placed on the right-hand side alongside a color bar indicating the temperature level. The above result can be explained by the fact that a shorter HHE receives more uniform heating under the same heating conditions, leading to the onset of oscillation at lower temperatures. In the following tests, the 10 cm length HHE is used because it can operate over a wide

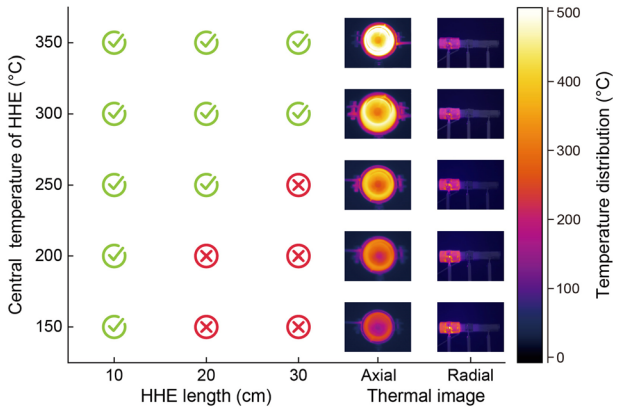

FIG. 2. The oscillation onset status in relation to the HHE length at different temperatures is depicted on the left-hand side: Green check marks (√) indicate successful oscillation onset, while red crosses (×) denote failures. The thermal images of the HHE from the axial and radial directions of the entire setup are placed on the right-hand side, alongside a color bar indicating the temperature level.

temperature range. Figure 3 illustrates the effects of varying heating temperatures (i.e., 150, 200, 250, 300, and 350 °C) on V_{oc} of the TAEH-TENG as well as the corresponding frequencies. Figure 3(a) demonstrates that V_{oc} increases monotonically as the heating temperature rises, showing a clear positive correlation between the temperature and voltage. Figure 3(b) shows a single waveform of the voltage signal at the corresponding temperature, exhibiting a growth trend in peak-to-peak voltage value that aligns with Fig. 3(a). As depicted in Fig. 3(c), as the temperature rises from 150 to 350 °C, V_{oc} increases from 17 to 25 V, and V_{RMS} from 11.08 to 14.93 V. This is attributed to the intensified vibration of the piston at high temperatures. The dominant frequency from the FFT analysis remains around 30 Hz, indicating the TAEH-TENG's ability to maintain stable performance even with increased excitations. This resilience highlights the robustness of the TAE when integrated with the H-TENG for diverse thermal applications.

Further analyses of the TAEH-TENG's performance under different thermal conditions are carried out, with the results detailed in Fig. 4. As the heating temperature rises from 150 to 350 °C, the peak and RMS currents increase from 1.38 and 0.50 μA to 3.30 and 0.98 μA, respectively, as shown in Fig. 4(a). The amount of transferred charge of the H-TENG fluctuates during temperature changes, yet the peak-to-peak value consistently exceeds 5 nC. Waveforms of the H-TENG's current and transfer charge at different temperatures are presented in Figs. 4(b) and 4(c). Subsequently, a resistance impedance matching test is conducted. At a heater temperature of 350 °C, a rheostat is used as an external load to evaluate the power output of the H-TENG. The voltage–resistance and power–resistance relationships are depicted in Fig. 4(d). During operation, the piston vibrates at an amplitude of approximately 5 cm and a frequency of about 29.5 Hz. The maximum power of approximately 0.48 mW is attained when the external load resistance is about 80 MΩ.

Subsequently, the performance of the TAEH-TENG is evaluated through a capacitor charging test. As illustrated in Fig. 4(e), the TAE with single H-TENG can charge the capacitors of 1, 3.3, 4.7, and 10 μF to 2.99, 1.69, 1.29, and 0.53 V, respectively, within 15 s. The unique

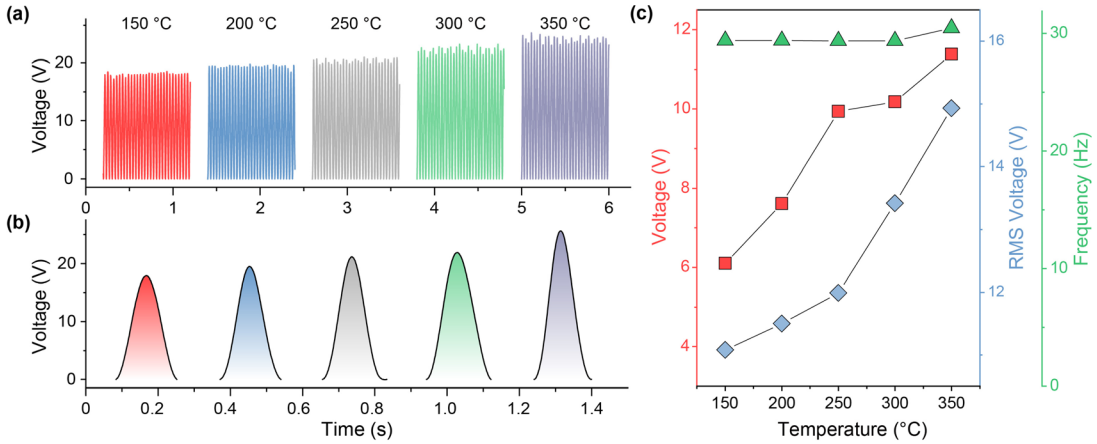

FIG. 3. Electrical performance of the TAEH-TENG at various heating temperatures with an HHE length of 10 cm. (a) Open-circuit voltage waveforms of the TAEH-TENG at different heating temperatures. (b) A single waveform under magnification. (c) The voltage, RMS voltage, and dominant frequency (obtained from the FFT analysis) vs the temperature.

structure of the H-TENG allows for easy deployment and stacking within the piston. To augment power output and enhance capacitor charging efficiency, four H-TENG units are stacked in the piston to boost power output and improve capacitor charging performance. The corresponding charging histories are plotted in Fig. 4(f). It is noted that the charging voltage of the 1 μF capacitor rises rapidly and stabilizes in about 12 s. Its saturation voltage is about 17.39 V. Under the same condition, the charging speed decreases as the capacitance increases. In 20 s, the voltages across the 3.3, 4.7, and 10 μF capacitors reach 8.37, 6.21, and 4.47 V, respectively. The results suggest that the TAE and H-TENG combination is effective in generating electricity.

Although the TAE and H-TENG combination can efficiently convert thermal energy into electricity, customized peripheral circuits are still necessary for efficient energy management to ultimately power

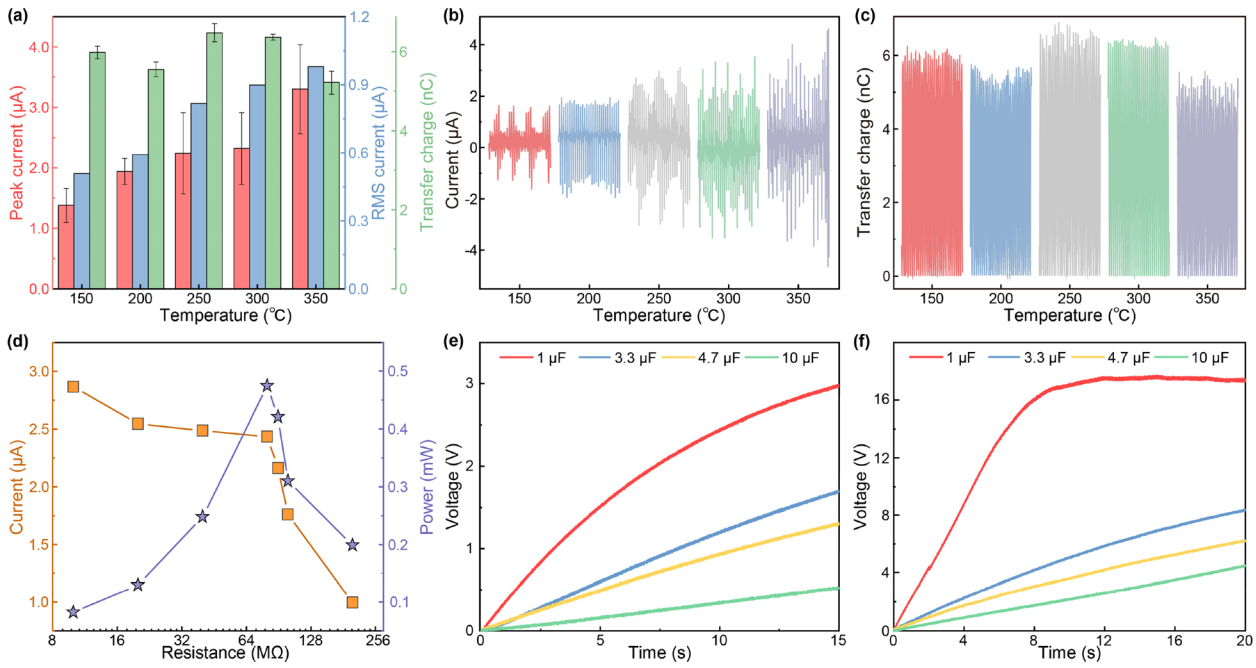

FIG. 4. Electrical performance of the TAEH-TENG at various heating temperatures with an HHE length of 10 cm. (a) Peak current, RMS current, and transfer charge at different heating temperatures (150, 200, 250, 300, and 350 °C), presented as mean values ± SD. (b) Current waveforms at varying heating temperatures. (c) Transfer charge profiles as a function of the heating temperature. (d) Dependence of power on the external load resistance for the TAEH-TENG operating at a heating temperature of 350 °C. Capacitor charging history of one H-TENG unit (e) and four H-TENG units (f).

real electronics. For this purpose, we developed a practical test platform, as illustrated in Fig. 5(a), which showcases the physical layout of the testbed, including essential equipment used for measuring and evaluating the system's performance. Figure 5(b) shows the photograph of the ultra-low-power Internet of Things (IoT) node, which is central to testing the harvester's effectiveness in real-world scenarios. This IoT node integrates a temperature sensor (TS) and a Bluetooth Low Energy (BLE) module. The receiving end employs an ESP32 microcontroller to enable cloud uploads, simulating practical usage conditions in an experimental framework.

The overall architecture of this testing platform, depicted in Fig. 5(c), demonstrates the flow of harvested energy through the rectifier, a 22 μF storage capacitor, and the LTC3588 energy management chip. This setup ensures a stable voltage supply for downstream circuits, which is crucial for reliable power management and efficient operation. Once the capacitor voltage exceeds the under-voltage lockout (UVLO) threshold of the LTC3588, it regulates a 3.3 V output until the voltage drops below 3.18 V. Then, the ultra-low-power IoT node starts working, detecting ambient temperature and transmitting the data wirelessly to the receiving end via BLE. The ESP32 microcontroller receives the signals and then uploads the data to an IoT cloud server. Figures 5(d)–5(f) illustrate the time-history voltage response throughout the initial and subsequent charging phases. Specifically, Fig. 5(d) depicts the repeated charge–discharge cycles of the self-powered sensing process. During the initial cold-start, the charging capacitor begins at zero voltage, takes 55 s to charge up to 4.8 V, and then proceeds to conduct the first wireless sensing task. Subsequent warm-starts take an average of 16 s, as indicated in Fig. 5(e), with five self-powered sensing tasks being completed in 120 s. Figure 5(f) shows that the discharging process lasts about 0.066 s. The voltage starts from

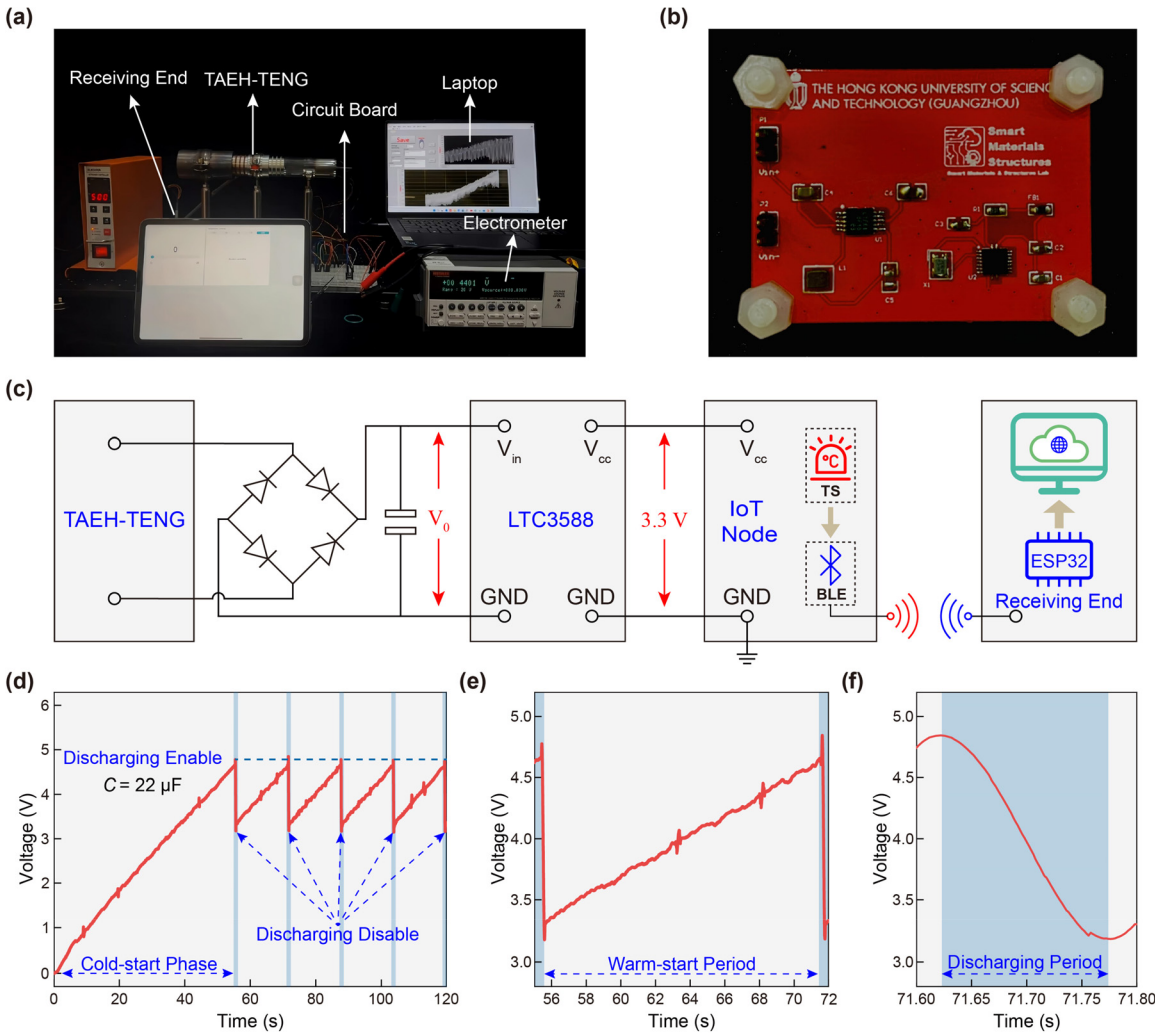

FIG. 5. Application demonstration and performance evaluation of the TAEH-TENG system. (a) Physical layout of the testbed. (b) Photograph of the designed ultra-low-power IoT node. (c) The integrated system architecture, illustrating the flow of harvested energy through the rectifier bridge, a 22 μF storage capacitor, the LTC3588 energy management chip, the IoT node, and the receiver. (d) Voltage profile of the 22 μF capacitor during multiple charging and discharging cycles. (e) The voltage across the storage capacitor rises during the warm-start phase. (f) Voltage response during the discharging phase.

4.86 V and decreases to 3.18 V, releasing 148.48 μJ of energy. This demonstration validates the integration of the TAE and TENG technologies, confirming the efficacy of the TAE and H-TENG combination for practical IoT applications. In Video S1, the application is showcased at a heating temperature of 500 °C. *In situ* temperature information can be monitored and transmitted wirelessly to the cloud, allowing users to access the data remotely from any location.

In this work, we have designed a honeycomb-structured triboelectric nanogenerator and integrated it with a thermoacoustic engine for energy harvesting. A parametric study was conducted on the HHE to explore the TAE's effective oscillation temperature range. At a heating temperature of 500 °C, the H-TENG achieved a maximum open-circuit voltage of 25 V, a peak current of 3.30 μA, an RMS current of 0.98 μA, and a peak power of 0.48 mW at an optimal impedance of 80 MΩ. Moreover, a 10 μF capacitor could be charged to 17.39 V in 12 s with four H-TENG units, storing about 1.51 mJ of energy. Furthermore, an ultra-low-power IoT node was developed to demonstrate the proposed harvester's value. Operating at a heating temperature of 500 °C, the integration of the TAE and four H-TENG units enabled self-powered *in situ* temperature monitoring, with the collected data being promptly uploaded to the cloud. This study represents a pioneering effort to demonstrate and prove that a thermoacoustic-based triboelectric energy harvesting system can effectively power a real-world IoT device. The results and findings have affirmed the potential of the proposed methodology for realizing self-powered nodes for various IoT applications.

See the supplementary material video S1 for an application demonstration and performance evaluation of the TAEH-TENG system.

This work was supported by the National Natural Science Foundation of China (Grant No. 52305135), the Guangdong Provincial Key Lab of Integrated Communication, Sensing and Computation for Ubiquitous Internet of Things (Grant No.2023B1212010007), the Guangzhou Municipal Science and Technology Project (Grant No. 2023A03J0011), and the Guangzhou Municipal Key Laboratory on Future Networked Systems (Grant No. 024A03J0623).

AUTHOR DECLARATIONS

Conflict of Interest

The authors have no conflicts to disclose.

Author Contributions

Yizhou Li and Yawei Wang contributed equally to this work.

Yizhou Li: Data curation (equal); Formal analysis (equal); Investigation (equal); Methodology (equal); Software (lead); Validation (equal); Visualization (lead); Writing – original draft (equal). **Yawei Wang:** Conceptualization (supporting), Data curation (equal); Formal analysis (equal); Investigation (equal); Methodology (equal); Software (supporting); Validation (equal); Visualization (supporting); Writing – original draft (equal). **Yihao Li:** Data curation (supporting); Formal analysis (supporting); Investigation (supporting); Methodology (supporting); Visualization (supporting). **Xuzhang Peng:** Formal analysis (supporting); Investigation (supporting); Methodology (supporting); Software (supporting). **Dian Li:** Investigation (supporting); Methodology (supporting). **Xin Xia:** Writing -review & editing (supporting). **Xin Li:** Methodology (supporting); Writing -review & editing (supporting). **Yunlong Zi:** Writing -review & editing (supporting). **Guobiao Hu:** Conceptualization (lead); Formal analysis (equal); Funding acquisition (lead); Investigation (equal); Methodology (equal); Project administration (lead); Supervision (lead); Writing -review & editing (lead).

DATA AVAILABILITY

The data that support the findings of this study are available from the corresponding author upon reasonable request.

REFERENCES

[1]S. Zhu, B. Peng, D. Li, Y. Bai, X. Liu, and Y. Li, E3S Web Conf. **512**, 04015 (2024).
[2]S. Zhu, D. Zhao, and Y. Li, J. Clean. Prod. **449**, 141839 (2024).
[3]J. Zuo, L. Dong, F. Yang, Z. Guo, T. Wang, and L. Zuo, Renewable Energy **202**, 56 (2023).
[4]F. Tohidi, S. G. Holagh, and A. Chitsaz, Appl. Therm. Eng. **201**, 117793 (2022).
[5]A. Ramkumar and M. Ramakrishnan, Mater. Today: Proc. **66**, 1552 (2022).
[6]A. W. Avent and C. R. Bowen, J. Acoust. Soc. Am. **137**, 2403 (2015).
[7]G. Chen, L. Tang, Z. Yang, K. Tao, and Z. Yu, Int. J. Energy Res. **44**, 2298 (2020).
[8]M. A. Timmer, K. de Blok, and T. H. van der Meer, J. Acoust. Soc. Am. **143**, 841 (2018).
[9]G. W. Swift, J. Acoust. Soc. Am. **84**, 1145 (1988).
[10]M. A. Pillai and E. Deenadayalan, Int. J. Precis. Eng. Manuf. **15**, 949 (2014).
[11]Y. Hu, Z. Jiang, K. Luo, D. Zhao, Y. Chen, G. Chen, E. Luo, and J. Xu, Energy Convers. Manage. **314**, 118662 (2024).
[12]W. B. Nader, J. Chamoun, and C. Dumand, Energy Convers. Manage. **215**, 112912 (2020).
[13]Y. Hu, K. Luo, D. Zhao, Z. Wu, Y. Yang, E. Luo, and J. Xu, Energy Built Environ. **5**, 628 (2024).
[14]G. Chen, S. Tao, R. Liang, Z. Li, W. Sun, J. Xu, and Z. Yu, Appl. Therm. Eng. **238**, 122047 (2024).
[15]C. R. Saha, P. H. Riley, J. Paul, Z. Yu, A. J. Jaworski, and C. M. Johnson, Sens. Actuators, A **178**, 179 (2012).
[16]H. Kang, P. Cheng, Z. Yu, and H. Zheng, Appl. Energy **137**, 9 (2015).
[17]R. Yang, J. Wang, Z. Wu, B. Huang, and E. Luo, Energy **263**, 125647 (2023).
[18]M. Elhawary, A. H. Ibrahim, A. S. Sabry, and E. Abdel-Rahman, Renewable Energy **159**, 414 (2020).
[19]V. Rohatgi, Bull. Mater. Sci. **6**, 71 (1984).
[20]L. Elias and A. C. Hegde, J. Alloys Compd. **712**, 618 (2017).
[21]M. A. Timmer and T. H. Van Der Meer, J. Acoust. Soc. Am. **146**, 3524 (2019).
[22]U. Ali, O. Al-Mufti, and I. Janajreh, Energy Nexus **15**, 100320 (2024).
[23]C. Iniesta, J. L. Olazagoitia, J. Vinolas, and J. Aranceta, Proc. Inst. Mech. Eng., Part A **232**, 940 (2018).
[24]G. Chen, L. Tang, and B. R. Mace, Appl. Therm. Eng. **150**, 532 (2019).
[25]J. Wang, Y. Zhang, M. Liu, and G. Hu, Int. J. Mech. Sci. **242**, 108016 (2023).
[26]Z. L. Wang, Faraday Discuss **176**, 447 (2014).
[27]Y. Wang, H. Du, H. Yang, Z. Xi, C. Zhao, Z. Qian, X. Chuai, X. Peng, H. Yu, and Y. Zhang, Nat. Commun. **15**, 6834 (2024).
[28]Y. Wang, X. Liu, Y. Wang, H. Wang, H. Wang, S. L. Zhang, T. Zhao, M. Xu, and Z. L. Wang, ACS Nano **15**, 15700 (2021).
[29]N. Sezer and M. Koç, Nano Energy **80**, 105567 (2021).
[30]W. Xu, M.-C. Wong, and J. Hao, Nano Energy **55**, 203 (2019).
[31]Y. Wang, Z. Hu, J. Wang, X. Liu, Q. Shi, Y. Wang, L. Qiao, Y. Li, H. Yang, J. Liu, L. Zhou, Z. Yang, C. Lee, and M. Xu, ACS Appl. Mater. Interfaces **14**, 24832 (2022).
[32]R. Guo, X. Xia, H. Luo, D. Zhang, and Y. Zi, Energy Environ. Sci. **17**, 5283 (2024).
[33]J. Fu, X. Xia, G. Xu, X. Li, and Y. Zi, ACS Nano **13**, 13257 (2019).
[34]A. Rajabi-Abhari, P. Li, M. H. Bagheri, A. A. Khan, C. Hao, N. R. Tanguy, D. Ban, L. Yu, and N. Yan, Nano Energy **131**, 110306 (2024).

[35]P. Yadav, K. Sahay, A. Verma, D. Maurya, and B. Yadav, Sustainable Energy Fuels **7**, 3796 (2023).
[36]S. Zhu, A. Yu, G. Yu, Y. Liu, J. Zhai, W. Dai, and E. Luo, Appl. Phys. Lett. **111**, 153901 (2017).
[37]S. Zhu, G. Yu, W. Tang, J. Hu, and E. Luo, Appl. Phys. Lett. **118**, 113902 (2021).
[38]F. Ahmed, G. Yu, and E. Luo, Energy Convers. Manage. **276**, 116482 (2023).
[39]G. Chen, L. Tang, and B. R. Mace, Int. J. Heat Mass Transfer **123**, 367 (2018).
[40]H. Yu, Z. Xi, H. Du, H. Yang, Z. Qian, X. Guo, Y. Guo, Y. Huang, T. Du, and M. Xu, Adv. Energy Mater. **14**, 2400585 (2024).
[41]C.-H. Cheng and H.-S. Yang, Energy **49**, 218 (2013).
[42]J. Xu, J. Hu, E. Luo, J. Hu, L. Zhang, and S. Hochgreb, Appl. Energy **305**, 117904 (2022).
[43]H.-S. Yang and C.-H. Cheng, Appl. Therm. Eng. **106**, 712 (2016).
[44]X. Xiao, X. Zhang, S. Wang, H. Ouyang, P. Chen, L. Song, H. Yuan, Y. Ji, P. Wang, and Z. Li, Adv. Energy Mater. **9**, 1902460 (2019).
[45]S. Niu, Y. Liu, X. Chen, S. Wang, Y. S. Zhou, L. Lin, Y. Xie, and Z. L. Wang, Nano Energy **12**, 760 (2015).
[46]H.-S. Yang and C.-H. Cheng, Int. J. Heat Mass Transfer **111**, 191 (2017).